X-RAY COMPUTED-TOMOGRAPHY OBSERVATIONS OF WATER FLOW THROUGH ANISOTROPIC METHANE HYDRATE-BEARING SAND

Yongkoo Seol[1] and Timothy J. Kneafsey[2]
[1]National Energy Technology Laboratory and [2]Lawrence Berkeley National Laboratory

Abstract

We used x-ray computed tomography (CT) to image and quantify the effect of a heterogeneous sand grain-size distribution on the formation and dissociation of methane hydrate, as well as the effect on water flow through the heterogeneous hydrate-bearing sand. A 28 cm long sand column was packed with several segments having vertical and horizontal layers with sands of different grain-size distributions. During the hydrate formation, water redistribution occurred. Observations of water flow through the hydrate-bearing sands showed that water was imbibed more readily into the fine sand, and that higher hydrate saturation increased water imbibition in the coarse sand due to increased capillary strength. Hydrate dissociation induced by depressurization resulted in different flow patterns with the different grain sizes and hydrate saturations, but the relationships between dissociation rates and the grain sizes could not be identified using the CT images. The formation, presence, and dissociation of hydrate in the pore space dramatically impacts water saturation and flow in the system.

***Keywords**: methane hydrate, anisotropy, x-ray computed tomography, capillary strength*

INTRODUCTION

Methane hydrate is an ice-like crystalline solid that typically forms from methane and water at high pressures and low temperatures. It can be found at and below the ocean floor and in deposits underlying permafrost where the thermodynamic conditions are compatible with hydrate stability (Sloan, 1998). Hydrates have recently attracted attention as a possible energy resource (e.g., Makogon 1987; Gornitz and Fung, 1994;

Holbrook et al., 1996; Kvenvolden, 1999; Buffet and Archer, 2004; Borowski, 2004; Milkov, 2004; Klauda and Sandler, 2005; Ruppel 2007) and a potential cause of global warming via methane gas release (e.g., Brook et al., 1996; Severinghaus et al., 1998; Kennett et al., 2000; Behl et al., 2003; Ruppel, 2000; Malikov and Sassen, 2003; Reagan and Moridis, 2007). To assess the potential of hydrates as an energy resource or environmental hazard, the behavior of hydrates in sediments and water flow through hydrate-bearing sediments needs to be clearly understood. Clennell et al. (1999) suggested that as a result of capillarity, gas hydrate forms heterogeneously in sediments with varying textural and mineralogical properties. Heterogeneous hydrate saturation and distribution would affect capillary pressure and relative permeability of the hydrate-bearing sediment, and these effects on fluid flow through the sediment are not well documented.

Previous experiments have been performed to characterize the properties of hydrate-bearing sand, particularly the thermodynamic and hydrological properties (e.g. Gupta et al. 2006; Moridis et al., 2006; Handa and Stupin 1992; Huang and Fan 2005; Klapproth et al. 2006; Kneafsey et al., 2007; Lu and Matsumoto 2002; Santamarina et al., 2004; Waite et al., 2004; Uchida et al., 2004; Uchida et al., 2002). However, most of those studies either were limited to homogeneous media or assumed that the hydrate-bearing sediments are homogeneous.

We formed methane hydrate in a heterogeneous sand column with a prescribed grain-size distribution pattern to observe the effects of heterogeneity on hydrate formation, water

flow through the heterogeneous hydrate-bearing sand, and hydrate dissociation. Our sand pack contained two grain-size ranges of silica sand, providing a permeability and capillary pressure contrast between layers, and was packed in layers varying in direction with respect to gravity and the column axis (i.e., perpendicular or parallel). X-ray computed tomography (CT) scanning was used to gather high-resolution density data, which was then converted to porosity and phase saturations (water, hydrate, and gas). The observations and measurements generated from the experiments using the heterogeneous system will aid in refining conceptual models of gas and water flow in hydrate-bearing porous media, and in predicting how natural heterogeneity in hydrate-bearing reservoirs can affect natural gas production. In this paper, we present the experimental steps taken to observe flow behavior during hydrate formation and dissociation, describe the phenomena observed at each step, and summarize the major impacts of grain-size distribution heterogeneity and key factors on controlling the water and gas flow through hydrate-bearing sands.

EXPERIMENTAL METHOD

The experiment consisted of five phases: (1) sand column packing and flow-system setup; (2) methane hydrate formation; (3) water flooding; (4) hydrate dissociation by depressurization; and (5) column saturation with water and subsequent drying to provide density reference data for phase saturation calculations. CT scans were conducted to (1) image saturation changes upon hydrate formation and dissociation, (2) infer water and gas migration in response to hydrate formation and dissociation, and (3) observe water

flow through the heterogeneous hydrate-bearing sand. In addition, temperature, pressure, and differential pressure across the sample were measured to monitor the status of the hydrate formation or dissociation process in the core sample.

Sand Column and Flow System Preparation

The pressure vessel used in this experiment was a 76.2 mm inner diameter and 89 mm outer diameter aluminum tube with threaded stainless steel end caps (Figure 1). Prior to packing the pressure vessel, the outlet end cap – equipped with three Type-K thermocouples (Omega Engineering, Stamford CT), a 6.4 mm thick neoprene foam pad, and a 12.8 mm thick solid Teflon spacer (to provide a cushion and thermal insulation between the sample and the stainless steel end cap) – was attached to the vessel.

Sand (U.S. Silica F110, Berkeley Springs, WV) was sieved into two fractions: fine-grain sand (53–177 μm) and coarse-grain sand (177–295 μm). The sand was selected because of its rounded, regular grain shape. These two sand fractions were washed with deionized water and air-dried before use. Following drying, they were moistened with distilled deionized water, resulting in the mass ratio of water to sand of 0.066 for both sands.

The two sands were packed into the pressure vessel according to the layer configuration shown in Figure 2. The vessel was oriented vertically during packing, and the sand was carefully packed into the vessel from the outlet to the inlet end in approximately 1 cm thick lifts and tamped into place using various diameter rods to maximize packing uniformity. During packing, 0.6 cm steel tubes were placed over each thermocouple to

protect them from the packing blows. The tubes were raised by the lift thickness as each layer of sand was added. Upon filling the vessel to the appropriate level, we inserted a matching Teflon spacer and neoprene foam pad on the top of the sand pack followed by the stainless steel end cap. The resulting sand column was 282 mm in length and 76.2 mm in diameter. Finally, the packed pressure vessel was oriented horizontally and allowed to equilibrate for three days prior to making hydrate.

The sand column had five main segments (Figure 2). Proceeding from the inlet end, and given the final horizontal orientation of the column, they are (1) horizontal layers with coarse sand on top, (2) a thin fine-grain sand layer perpendicular to the vessel axis, (3) horizontal layers with fine-grain sand on top, (4) alternating fine/coarse/fine vertical layers perpendicular to the vessel axis, and (5) vertically divided layers with fine sand on the thermocouple side of the column. A fine sand layer at the inlet end was used to provide uniform flow to the sample, and a coarse sand layer was placed at the outlet end. The three thermocouples were situated on the boundary between the fine and coarse sands in the center, horizontally oriented segment.

The pressure vessel was fitted into a PVC water jacket, through which temperature-controlled water/ethylene glycol was circulated to control the system temperature. The inlet end of the pressure vessel was connected to a 3.8 L steel bottle, and an ISCO 500D syringe pump (Lincoln, NE) was used to control flow during the experiment. Both the bottle and the ISCO pump were connected to various gas cylinders (CH_4, N_2, or CO_2) when needed. The outlet end of the pressure vessel was also connected to an ISCO 500D

syringe pump and a backpressure regulator. Pressures were monitored at the two pumps, the vessel inlet, and the differential pressure across the sample, while temperatures were measured using Type-K thermocouples in the room, the temperature-controlled bath, the sample at three locations, and the bottle containing methane gas.

The pressure vessel with the water jacket was insulated to minimize external thermal influences and mounted on the x-ray CT scanner table to reduce table-positioning errors. A modified Siemens HiQ medical x-ray CT scanner was used to obtain CT images. Sequential 10 mm thick cross-sectional images were collected over the length of the sample (28 slices). The voxel size for the CT images for this test was ~0.24 × 0.24 × 10 mm; 371 × 371 voxels per slice are presented in the images shown. The CT scans were performed periodically, including before and after hydrate formation, during the water flooding, during dissociation, while the sample was water-saturated, and while it was completely dry.

Figure 3 presents the 28 CT images comprising the sample, showing the initial condition and the horizontal or vertical layer boundaries as specified in Figure 2. Each voxel of the CT images represents the average density for a 1 cm slice of the sand calibrated from materials with known density. The varying density shown in the images resulted from slight non-uniform packing and variations in water saturation due to corresponding variations in capillary strength. Here we refer to capillary strength as a measure of the tendency for a material to imbibe a wetting fluid (in this case water). Capillary strength increases in regions with tighter grain packing and in sand with smaller grain sizes,

resulting in higher water saturation in these regions. Small white circles appearing in the interior of the Slices 14 through 28 identify the three thermocouples, which sense temperature at the tip of wire. Calculated from the CT images, the average initial porosity ranged between 0.34 and 0.37, and the average water saturation ranged between 0.18 and 0.40 (Table 1, Figure 4).

Hydrate Formation

Hydrate was formed by chilling and pressurizing the sample column to an appropriate temperature and pressure within the hydrate stability region. We initially set the temperature to 4^{o}C and the methane gas pressure to 4.8 MPa (700 psi) to form the hydrate, but because hydrate did not begin to form in two days, we lowered the temperature to 3ºC and raised the methane gas pressure to 5.5 MPa (802 psi) to expedite the hydrate-forming process. Hydrate began to form about 12 hours after the change in conditions. The completion of hydrate formation was identified by constant pressure and temperature inside the pressure vessel. During hydrate formation, the pressure vessel was connected to the 3.8 L methane gas reservoir having a known temperature, and the quantification of the hydrate formed was calculated from the number of moles of methane removed from the gas phase (i.e., pressure decrease), using appropriate volumes, pressures, temperatures, and methane properties from Lemmon et al. (2005). After hydrate formed, average gas permeability on the entire column was measured (Table 1).

Figure 5a shows temperature and pressure during the hydrate formation period. Hydrate formation was inferred from the concomitant temperature rise and pressure drop caused

by the exothermic reaction. The formation was not steady, resulting in several temperature peaks, and at completion, the temperature stabilized. Figure 6 shows hydrate saturation following formation. Hydrate saturation was calculated based on the x-ray attenuation values, which were compared to fully water-saturated and completely dried sand CT images collected later (Figure 12). Figure 7 shows the average hydrate and water saturations in each slice for each sand following hydrate formation, which are also shown in Table 1.

Water Flood

Deionized water was injected into the sand column at a rate of 4.0 mL/min using the syringe pump. Injected water was not presaturated with methane, and water temperature was not separately controlled, because it was expected that the water would be thermally equilibrated while flowing through the massive temperature-controlled pressure vessel end piece. During the water flood, CT scans were taken at three specific locations (Slices 7, 13, and 23) rather than throughout the entire column, with the observed slices representing each of the main column segments. The changes in water saturation as the water flood progressed were calculated based on the assumption that the hydrate present in the sand column was stable – neither forming nor dissociating as the temperature-pressure conditions were constant and within the hydrate stability region (3ºC and 700 psi). Some hydrate dissolution into water would occur during the water flood (Redher et al., 2004), but was not expected to be significant for this study.

Hydrate Dissociation

Hydrate dissociation was initiated by slowly lowering the sample pressure and attempting to avoid the formation of ice. We used a back-pressure regulator to control pressure during hydrate dissociation. The outflow from the vessel (mostly gas with a small quantity of water) was flowed to a Marriott collection bottle for gas quantification. Before depressurization, the pressure inside the vessel was 691 psi (4.76 MPa). The pressure was set at 520 psi (3.59 MPa) to initiate the dissociation, further adjusted to 400 psi (with a brief low-pressure overshoot), and later lowered stepwise until the inside pressure was close to atmospheric (Figure 5b). During dissociation, x-ray CT scans of every other slice over the entire sample were performed regularly (14 slices). The sample was scanned every 10 to 13 minutes to monitor the changes in density, indicating changes in hydrate, gas, and water saturations.

Saturated and Dry Sand Column

CT images of the sand column while completely water-saturated and completely dry provide the best endpoints for computing hydrate and fluid saturations during other stages of the experiment. For this purpose, after hydrate formation, water flooding and dissociation, the sand column was fully saturated with water, scanned, completely dried, and scanned again. Note that during the water saturation, some gas was unintentionally injected into the column, causing gas bubbles to disturb the sand packing in the first few slices. This in turn impacted the calibrations in the disturbed region in those affected slices, as shown in Figures 6, 8, 10, and 13.

RESULTS and DISCUSSION

Sand Column

Table 1 shows the average porosities and fluid saturations calculated from the CT images. The porosity of the coarse sand is lower than that of the fine sand, and consequently the bulk density of the coarse sand is higher than the fine sand. However, the average water saturation (0.40) in the fine sand is much higher (Figure 4 and Table 1), because of the higher capillary strength compared to the coarse sand (0.178).

Hydrate Formation

The hydrate saturation in the fine sand exceeded that in the coarse sand (Table 1 and Figures 6 and 7). This finding was expected, because hydrate saturation is closely related to the initial water saturation, and because the initial water saturation in the fine sand is significantly greater than that of the coarse sand. However, in the fine sand, the hydrate saturation (0.358) was less than the expected hydrate saturation (0.388) calculated from the consumed water saturation (0.400–0.093=0.307) and volume expansion that occurs when methane is added to a volume of water to form hydrate (factor of 1.265). In the coarse sand, the hydrate saturation (0.270) was higher than the expected hydrate saturation (0.130). These observations confirm that as hydrate forms, water redistributes according to changing capillary strengths (Kneafsey et al., 2005; Gupta et al., 2006; Kneafsey et al., 2007), and that hydrate formation caused imbibition of water to regions where the sand was initially drier.

One possible explanation for the lower-than-expected hydrate saturation in the fine sand is that the fine sand (because it has smaller pores) initially has higher capillary strength and also has lower intrinsic permeability than the coarse sand. The capillary strength of the sand will increase with hydrate formation because hydrate is a water-wetting solid occupying pore space, thus making pores smaller. Pore clogging could occur if hydrate builds up in a pore and hinders water and gas flowing through the pores, and the fine sand is more susceptible to the pore-clogging effects of hydrate. Extensive hydrate formation at a location could reduce porosity enough to hinder the flow of gas, resulting in not all available water being transformed into hydrate, owing to the shortage of methane gas. This pore clogging would occur more likely in the fine sand, because of the smaller pore size. Pore clogging may impede water flow in the fine sand, allowing the water to be drawn into the coarse sand, where less pore clogging would be expected.

Figure 6 shows the CT images collected following hydrate formation, and Figure 7 shows the average saturations of hydrate and water in each slice. Hydrate saturation is more uniform in the coarse sand, but more highly localized in the fine sand. The fine sand contains a much less hydrate-saturated region below the highly concentrated hydrate region (e.g. Figure 6, Slices 5 and 12, where is a dark region appears beneath the bright region in the fine sand). The average hydrate saturation is highest (~53% at Slice 10) in the fine sand of the middle segment and decreases to below 30% at Slice 15 (also in this segment). Average hydrate saturation in the coarse sand ranges from about 30 to 50% in the first segment and 17 to 20% in the rest of the column, except for Slices 15, 18, and 19, located at the boundary with fine sand. The highest hydrate saturation in the coarse sand

(44%) was found in the vertical layer (Slices 18 and 19) located between the two vertical fine layers in the middle of the column. This layer had the highest initial water saturation for the coarse sand as well.

Images of hydrate saturation in Figure 6 suggest that there exist three contrasting regions in the column in terms of hydrate saturation, one from Slice 1 to 15, another from Slice 16 to 21, and the other from Slice 22 to 28. In the first region, hydrate forms in circular band-shaped as half rings, while in the other two regions, the hydrate is generally locally concentrated (e.g., Slice 17 and 18) or disseminated (e.g., Slice 23 to 27). The complex patterns of hydrate distribution observed during hydrate formation are still incompletely understood. It is possible that the dominant water-migration directions might be different in the different regions, with (1) radial (i.e., normal to column axis) migration dominant in the first region resulting in the circular band pattern of hydrate saturation, (2) axial – i.e., parallel to column axis– migration in the second region **(**causing locally intensive hydrate formation), and (3) less active migration in the third region resulting in a more uniform hydrate distribution.

While the circular- band-like hydrate formation has been observed in other experiments (Kneafsey et al., 2007), the mechanism causing this is not completely understood either. However, this behavior may be similar to ice-lens formation in permafrost regions (Davis, 2001). When forming, the higher hydrate saturation zones must have both adequate heat transfer and the ability to draw in water from neighboring regions. If we assume that hydrates were to begin forming everywhere simultaneously, the temperature of the

sample would at first increase uniformly. The region closest to the vessel wall would cool, because it has the best heat transfer, and hydrate would form there. Hydrate formation would proceed from the vessel wall inwards. In the center, the temperature would still be relatively high, because of the distance to the vessel wall where the temperature is controlled. At some intermediate radius, heat transfer would be adequate to keep temperature low enough for hydrate formation, with the rate of heat transfer comparable to the heat released upon hydrate formation. Water would be drawn to this location by capillarity from the warmer center, thus creating a locally high-hydrate-saturation band and a lower hydrate saturation center. Geological medium and hydrate-saturation heterogeneity would affect the circularity of this region, because they alter heat and water flow.

Slices 10 to 15 in Figure 6 show a similar concentrated hydrate zone (bright band) and water-depleted zone (dark region) in the fine sand. However, the coarse sand did not show a high hydrate-saturation band. Instead, a crack-like low-density area extending through Slice 21 formed. According to the densities estimated from the CT images, this narrow crack-like region is not void space, but a low-density area. The density in the crack region was about 1.62 g/cm^3, whereas the density of the dry sand in the same area was about 1.72 g/cm^3. It may be a region where water was depleted, lowering capillary adhesion between grains, so that water could not hold the sand particles together. The crack could have resulted from the migration of water from the region near the crack to the location where hydrate was forming. The low-density dark zone around the crack-like region suggests intensive water depletion there. The crack would not act as a water

migration pathway under capillary driven conditions; however, under pressure-driven conditions, it might act as a primary conduit for the flow of water and possibly gas or water vapor.

The expected hydrate saturation in the coarse sand in Slice 18 (based on the initial water saturation and residual water saturation) would be about 13% (Figure 4), but the actual hydrate saturation is about 31% (Figure 7). These findings indicate that a significant volume of water migrated into the coarse region here. In the segment between Slices 22 and 27, the boundary separating the different grain-size sands has a lower density than the surrounding sands which could result in similar fluid-flow behavior as in the crack-like region in Slices 10 to 21. The circular-banded hydrate formation pattern was not observed here. Water in the fine sand likely migrated into the alternating vertical layers (Slices 17 to 21) where the hydrate saturation was higher than expected (Figure 7), but fluid migration within the coarse sand of the segment was minor, so that the hydrate distribution resulted in a rather uniform hydrate distribution.

The observations of hydrate formation indicate that it is controlled by the availability of gas, water, and heat transfer, and as hydrate formed, the components were dynamically redistributed according to saturation, the gradient of capillary strength, and the relative permeability of each phase.

Water Flood

We monitored the water flood using CT scanning to identify the dominant flow pathways through the hydrate-bearing sands. Information on water flow through such heterogeneous hydrate-bearing sediment enhances our understanding on the flow of water released from hydrate dissociation when a hydrate reservoir is under development for natural gas.

Figure 8 shows the changes in water saturation during the waterflood at three locations. These locations were selected to examine the effects of grain size, hydrate saturation, and gravity on water flow through the regions having coarse and fine layers aligned parallel to the column axial direction. Water-saturation breakthrough curves for the three locations calculated from the CT data are shown in Figure 9. Vertical fine sand layers placed between the three major column segments were designed to act as flow buffer zones, providing relatively uniform water inflow to subsequent column segments. However, the hydrate saturation in these layers was observed to be heterogeneous as well, with the distributions resembling those of the nearby segments. Thus, the uniform flow redistribution was unlikely.

The top 11 images in Figure 8 show the water saturation changes in the segment (Slice 7) having the coarse sand over the fine sand with a nearly horizontal boundary. The initial hydrate distribution is shown in the first image as a relatively brighter (purple) region. In the lower fine sand, there is a narrow band of high hydrate saturation bounded by a water/hydrate-depleted low-density zone, whereas the hydrate is distributed more uniformly, with a wider circular band in the upper coarse sand. The inflow of water

appeared in the fine sand at around 30 minutes. after injection, directly beneath the high-hydrate-saturation zone in the water/hydrate-depleted zone, where permeability would be higher (see also Figure 9) and the capillary strength influenced by the high hydrate saturation immediately above. Water first filled the lower fine sand and then, later, slowly imbibed upward into the coarse sand, more readily through the higher hydrate-saturation zone, which had increased capillary strength (dotted arrows). A low-density (dark) region in the center of the column remained nearly unsaturated (trapped gas) after water was fully introduced into the rest of column. The central low-density region may have resulted from rearrangement of sand particles as hydrate formed, or from gas trapped by flow-path blockages caused by residual water or hydrate formed at pore throats.

The center set of images in Figure 8 shows the flow pattern in the horizontal layers of the second segment (Slice 13), with the upper fine-grain sand. The water breakthrough first appeared in the fine sand just beneath the high hydrate-saturation region as had occurred in the first segment (Slice 7), and water slowly filled upwards around the high hydrate-saturation region. After the complete satiation of the fine-sand section, there was a slightly less saturated region remaining in the center of the high hydrate-saturation region, where the circular-band-shaped high-hydrate density region pinches out. This region seems isolated by what may be a pore-blocking hydrate formation from outside water flow. Water started to flow down to the lower coarse sand at around 50 minutes, primarily flowing along the pressure vessel wall, going around the main gas filled region. The low-density crack-like region found in the lower coarse sand started acting like a flow conduit at around 59 minutes. The lower coarse sand showed relatively uniform

water saturation except for the area with the crack-like region and the surroundings which ultimately had greater water saturations.

The lower set of images in Figure 8 (Slice 23) shows the water breakthrough in the sand layers having a vertical contact boundary with the fine sand on the left. Hydrate saturation in this segment was relatively uniform in both the fine and coarse sand, but slightly higher at the top-left region in the fine sand. The water breakthrough occurred in the center of the fine sand, directly beneath the higher hydrate-saturated sand where the hydrate saturation was lower. The vertical boundary between the two sands seems to impose a capillary barrier, hindering water flow between the two sides. After the fine sand was nearly satiated, the coarse sand started to fill up from the bottom. When the entire coarse sand section was nearly saturated, the top portion of the fine sand was still not yet fully saturated. The area would be similarly isolated by trapped gas or pore clogging with hydrate saturation, as shown in other slices (such as Slice 13).

Figure 9 shows the breakthrough curves of water at three locations at Slices 7, 13, and 23. The breakthrough curve for the fine sand for Slice 7 is steeper than the curve for the coarse sand, possibly because of the higher capillary strength in the fine sand. The coarse sand reaches about 60% water saturation (total saturation = hydrate saturation + water saturation = 95%), while the fine sand reaches higher than 70% (total saturation = ~100%) when the coarse sand sits on top of the fine sand, indicating that both gravitational and capillary forces are affecting the saturation. The breakthrough curves at the other two locations (Slices 13 and 23) showed clear contrast with those at the first

observation location (Slice 7) in terms of the slope and arrival time. The breakthrough curves at the two locations (Slices 13 and 23) showed faster increases in the slope of the curves for the coarse sand, and the time gap between the curves of the two sands is longer at the second location (Slice 13). Apparently, the geometric configuration of the two segments resulted in similar breakthrough curve slopes, and both gravitational and capillary forces were affecting the saturation. Because hydrate saturation in the fine sand was higher in the second segment, it is likely that the higher capillary strength in the fine sand was able to imbibe water earlier. Gravitational forces helped water flow into the coarse sands, so that the saturation in the coarse sand increased faster in the two segments (Slices 13 and 23) than in the first segment (Slice 7).

In general, the fine sand became satiated earlier due to the higher capillary strength. In all cases, the water initially appeared in the fine sand immediately beneath a higher hydrate-saturation region. This is probably because the higher permeability in the low-hydrate-saturation region (relative to the higher-hydrate-saturation region) provides less resistance to flow, whereas the higher capillary strength of the fine sand, further increased by hydrate saturation, retains the water. Gravitational force also affects the water breakthroughs through the sands, because the flow is located beneath the high hydrate-saturation region.

Hydrate Dissociation

We depressurized the system to induce hydrate dissociation in the water-satiated hydrate-bearing sand. During dissociation, there was no inflow through the inlet, and fluids were

removed through the outlet, so any gas generated from dissociation had to travel through the sample to the outlet to be produced. Hydrate dissociation requires heat input regardless of the method used. Depressurization causes the initial dissociation to occur throughout the sample from the heat already present in the sample before heat transfer from outside the sample is required. As hydrate dissociation progressed, we regularly captured CT images of alternate 10 mm slices.

Figure 10 shows the density ratio (mass of pore-filling phases [water, hydrate, gas] to mass of water at saturation – DR) of the sample monitored at five locations as the hydrate dissociated. At each location, six images at different times are shown to present the evolution of gas and water phase and the disappearance of the hydrate phase. In this figure, darker regions contain the less dense component (gas), and the brighter regions contain the denser components (hydrate or water). The figure is annotated with numbers indicating the location of interesting features that will be described in detail below.

During dissociation, regions having high hydrate concentration become darker because hydrate dissociation generates less dense gas. The first images on the top two rows (Slices 3 and 5) show circular bands of high hydrate-saturation region, which turn into darker bands as time progresses (images to the right). The high hydrate-saturation region become darker (higher gas saturation) faster in the coarse sand than the corresponding high hydrate-saturation region in the fine sand, where the high hydrate-concentration region (lighter region) persists longer. It is not clear if the variation would result from different dissociation rates from varying capillary strength of sands, heat transfer, or

different relative masses of hydrate or water. Higher capillary strength of the fine sand holds water tighter than gas as the hydrate releases water and gas.

In Slices 3 and 5, the gas released from hydrate dissociation in the more highly hydrate saturated region moves to the outer region through a narrow channel (Feature #1 in Slices 3 and 5) which appears to be a preferential gas flow path in the coarse sand. The gas from hydrate dissociation in the fine sand appears to flow preferably into the adjacent coarse sand (Feature #2 in Slices 3 and 5). In the coarse sand, the darker region near the boundary between the two sands (Feature #2 in Slices 13 and 25) would result from the similar gas flow released from the high hydrate-saturation region in fine sand.

In the fine sand, an irregular area of high density (i.e., high water saturation) appeares in the lower central region (Feature #3 in Slices 3 and 5). This region is in the same area where water was depleted during hydrate formation (see Figure 6) and then refilled with water during the water flood. Since the region contained little hydrate to begin with, it remained high in water saturation because little gas was produced there.

Hydrate dissociation is affected by heat transfer, and thus hydrate dissociation would occur more readily where heat can be easily transferred from the outside (near the vessel wall). Faster dissociation was observed on or near the contact with the aluminum vessel wall (Feature #4 in Slices 13 and 17). The outer region dissociates faster than the inner region in the circular-band region where the hydrate concentration is high (fine sand in Slice 13).

As the hydrate dissociated, the crack-like low-density region, which developed upon hydrate formation (Feature #5 in Slice 17 and Figure 5, Slices 10-21) disappeared. This disappearance may have resulted from the disaggregation of sand particles associated with hydrate and rearrangement of sand particles with fluid released from dissociating hydrate, or from water being reintroduced into this region after it had become extremely dry upon hydrate formation.

Figure 11 shows the variations in the DR over time at three locations during dissociation. Over time, the fine-sand DR becomes relatively uniform throughout the column, even though the initial DRs were varied. The coarse sand shows the opposite trend, with a varying final DR at different locations as time progressed. The varying final DR in the coarse sand suggests that the gas and water released from hydrate dissociation were pushed toward the outlet, whereas the inlet end remained more highly saturated with gas. The fine sand with a higher capillary strength retains a higher and more uniform water saturation than the coarse sand. The magnitude of the decline in DR is also different for each sand—the final DR in the fine sand is approximately 0.65, whereas the final DR in the coarse sand ranges from 0.43 to 0.6, indicating a greater accumulation of gas in the coarse sand. The slice-by-slice water saturations following hydrate dissociation are presented in Figure 12. From this figure, we can see that the final water saturation is decreasing in the first column segment (9 slices) and is quite uniform for the rest of column, and the water saturation of the coarse sand in the first segment of column

dropped to nearly 0.4 as a result of gas accumulation while the rest of column had water saturations close to 0.6.

The observations of varying hydrate and water saturations as hydrate dissociation progressed suggest that hydrate dissociation rates may vary with different grain sizes, permeability, and capillary strength. Hydrate dissociation may force the sand particles to be redistributed as fluid flows through the medium.

Column Saturation and Drying

The sand column was water saturated after hydrate dissociation and dried before unpacking. CT scans of the saturated and dried conditions were needed to calculate porosity and fluid saturations. Figure 13 shows the CT images of the odd slices taken after the water saturation (top) and drying (bottom). The images appear uniform except for the first several slices, where air was unintentionally injected during water saturation, causing local disturbances in the sample. The images also show no signs of permanent density changes resulting from hydrate formation or remnants of the crack.

SUMMARY

We designed and performed an experiment to observe hydrate formation and dissociation and water flow in sands with prescribed heterogeneity. A 28 cm long sand column was packed with several segments having vertical and horizontal sand layers with different grain sizes. The configuration was designed to investigate the impact of permeability

contrast, capillary-strength anisotropy, and gravity on fluid flow and the formation and dissociation of hydrate. Direct observation was possible using x-ray CT that nondestructively visualizes variations in density, from which fluid saturations and geological medium porosities can be calculated.

In our experiment, grain-size-distribution heterogeneity resulted in varying initial water saturation as capillary strength of different sands redistributed the water. We expected the fine sand to attain a higher initial water saturation than the coarse sand, because the fine sand should have a higher capillary strength. This was observed in the difference between our packing conditions (same gravimetric moisture content for both sands) and our initial conditions, in which the saturation in the fine sand greatly exceeded that of the coarse sand.

We would have predicted that the hydrate saturations in each sand would be proportional to the water saturation in each sand. This was not the case, however, as the resulting hydrate saturation in the coarse sand exceeded the expected saturation, whereas the hydrate saturation in the fine sand exceeded the expected saturation at some locations, matched it at others, and was exceeded by it elsewhere (vertical layers).

Hydrate saturation shows larger variation in the fine sand than the coarse sand, which was not expected. The interplay of heat transfer, capillary pressure, and water effective permeability during hydrate formation is responsible for this variation in hydrate saturation. At the start of hydrate formation, capillary pressure is the same in both fine

and coarse sands. Hydrate forming in the pore space will increase the capillary strength by making the pores smaller. Coarse sand has larger pores, lower water saturation, and probably lower water relative permeability than the fine sand. The thermal conductivity of the coarse sand will also be somewhat lower because less water is present.

When hydrate forms at a location in the sand, the pores become smaller, which results in higher capillary pressure drawing water towards the hydrate-forming location as heat dissipates away. The formation of the same amount of hydrate in both sands will cause the capillary pressure in the fine sand to increase more than in the coarse sand because of the relative pore sizes. In the fine sand, water will be imbibed more quickly to the hydrate because of the higher water effective permeability, and heat will be more rapidly conducted away, allowing for higher hydrate saturations to form. In the coarse sand, hydrate formation will result in a lower capillary strength than the fine, and both water and heat will be less mobile. This will result in the hydrate variation in the coarse sand having less variation.

During hydrate formation, as well as fluid (water or vapor) migration and heat flow, grain rearrangement may occur resulting from the depletion of cohesive water holding grains together, and a crack-like low density zone was developed. This low density region would not be conduit for water flow under capillary-driven flow conditions, but could be primary pathways for water, gas, and water vapor at pressure-driven flow conditions. As hydrate dissociated, the crack-like region disappeared as a result of disaggregation or rearrangement of sand particles. The low-density region did not leave permanent

remnants of density changes after the column had been water saturated and completely dried.

During the water flood, the hydrate presence would affect water flow in two ways: hindering flow and enhancing imbibition. The hydrate in the pore space will decrease permeability to advectively driven water hindering flow. It will also result in water being imbibed into remaining connected pore space, as the capillary strength is high enhancing imbibition. In the three regions studied, the water first appeared in low-hydrate-saturation regions (higher permeability) immediately beneath (gravity) higher hydrate-saturations (capillary strength). Water imbibes into the fine sand layer preferentially, but hydrate formation in fine sand could hinder the water flow through it by plugging flow paths and trapping gas bubbles. The hydrate formation in coarse sand enhances the water imbibition as capillary strength in the coarse sand increases with hydrate. The water flow we observed in hydrate-bearing sand was mainly capillary-force driven, while gravitational effects resulting from layer configuration were also noted when the saturated fine sand was located above or next to the coarse sand.

In our experiment, hydrate dissociation was initiated with depressurization and heat was supplied by the surrounding temperature-controlled fluid. Our observations could not verify that dissociation occurs at a faster rate with a specific sand but do verify that the dissociation occurs faster at or closer to the wall boundary through which heat is provided. Gas released from hydrate dissociation escaped from fine sand into coarse sand, and preferential pathways of gas flow were observed in coarse sand, and between layers of

sand elsewhere. The capillary strength of fine sand imbibed the released water into the fine sand, resulting in water saturation higher than that of coarse sand.

Changes in saturation, permeability, and capillary strength play significant roles as hydrate forms and dissociates. Grain-size-distribution heterogeneity provided an initial variation in capillary strength in the medium. The fact that all natural porous media have some degree of heterogeneity should be carefully considered before a hydrate system is simplified in numerical simulations, either for predictions of natural gas production from hydrate-bearing reservoirs, or for risk assessments regarding hydrate reservoir stability.

ACKNOWLEDGMENTS

The authors wish to acknowledge Michael Kowalsky, Matthew Reagan, and Dan Hawkes for their helpful comments in reviewing this manuscript. This work was supported by the Assistant Secretary for Fossil Energy, Office of Natural Gas and Petroleum Technology, through the National Energy Technology Laboratory, under the U.S. DOE Contract No. DE- AC02-05CH11231, and also in part by the Korean Institute of Geoscience and Mineral Resources.

REFERENCES

Behl, R. J., J. P. Kennett, K. G. Cannariato, and L. L. Hendy, 2003. Methane hydrates and climate change: The Clathrate Gun hypothesis, AAPG Bull., 87(10), 1693.

Borowski, W. S., 2004. A review of methane and gas hydrates in the dynamic, stratified system of the Blake Ridge region, offshore southeastern North America, Chem. Geol., 205, 311.

Brook, E. J., T. Sowers, and J. Orlando, 1996. Raid variations in atmospheric methane concentration during the past 110,000 years, Science, 273, 1087.

Buffett, B., and D. Archer, 2004. Global inventory of methane clathrate: Sensitivity to changes in environmental conditions, Earth Planet. Sci. Lett., 227, 185.

Clennel, M. B., M. Hovland, J. S. Booth, P. Henry, and W. J. Winters, 1999. Formation of natural gas hydrates in marine sediments 1. Conceptual model of gas hydrate

growth conditioned by host sediment properties, J. Geophys. Res. 104 (B10), 22985-23003

Davis, T. N. 2001. "Permafrost: A Guide to Frozen Ground in Transition", University of Alaska Press

Gupta A., T. J. Kneafsey, G. J. Moridis, Y. Seol, M.B. Kowalsky, and E. D. Sloan, Jr. 2006. Composite Thermal Conductivity in a Large Heterogeneous Porous Methane Hydrate Sample. *Phys. Chem. B*, 110 (33), 16384 -16392

Gornitz, V., and I. Fung, 1994. Potential distribution of methane hydrate in the world's oceans, Global Biogeochem. Cycles, 8, 335.

Holbrook,W. S., H. Hoskins, W. T. Wood, R. A. Stephen, and D. Lizarralde, 1996. Methane hydrate and free gas on the Blake Ridge from vertical seismic profiling, Science, 273, 1840.

Kennett, J. P., K. G. Cannariato, L. L. Hendy, and R. J. Behl, 2002. Methane Hydrates in Quaternary Climate Change: The Clathrate Gun Hypothesis, Spec. Publ., vol. 54, AGU, Washington, DC.

Kneafsey, T. J., L. Tomutsa, C. E. Taylor, A. Gupta, G. J. Moridis, B. M. Freifeld, and Y. Seol, 2005. Methane hydrate formation and dissociation in a partially saturated sand, The 229th ACS National Meeting, San Diego, CA.

Kneafsey, T. J., L. Tomutsa, G. J. Moridis, Y. Seol, B. M. Freifeld, C. E. Taylor, and A. Gupta, 2007. Methane Hydrate Formation and Dissociation in a Core-Scale Partially Saturated Sand Sample, Journal of Petroleum Science and Engineering, 56, 2007 108-126

Kvenvolden, K. A., 1999. Potential effects of gas hydrate on human welfare, Proc. Natl. Acad. Sci. U.S.A., 96, 3420.

Handa, Y.P. and D. Stupin, 1992. Thermodynamic properties and dissociation characteristics of methane and propane hydrates in 70A radius silica gel pores. J. Phys. Chem. 96, 8599

Huang, D. and Fan, S., 2005. Measuring and modeling thermal conductivity of gas hydrate-bearing sand. J. Geophys. Res. 110 (B01311).

Klapproth, A., K.S. Techmer, S. A. Klapp, M. M. Murshed, and W. F. Kuhs, 2006. "Microstructure of gas hydrates in porous media", Proceedings of the 11th International Conference on the Physics and Chemistry of Ice, Bremerhaven, July 23 - 28, 2006, Royal Society of Chemistry, ISBN: 10 digit - 0-8540-4350-0, 13 digit - 978-0-8540-4350-7

Klauda, J. B. and S. I. Sandler, 2005. Global distribution of methane hydrate in ocean sediment. Energy and Fuels, 19, 459.

Lemmon, E. W., M. O. McLinden, and D. G. Friend, 2003. Thermophysical properties of fluid systems. In: Linstrom, P.J., Mallard, W.G. (Eds.), NIST Chemistry WebBook, NIST Standard Reference Database. National Institute of Standards and Technology, Gaithersburg MD. http://webbook.nist.gov.

Lu, H. and R. Matsumoto, 2002. Preliminary experimental results of the stable P_T conditions of methane hydrate in a nannofossil-rich claystone column, Geochemical Journal, v 36, pp. 21-30

Makogon, Y. F., 1987. Gas hydrate: frozen energy, Recherche 18(192), 1192

Milkov, A. V. and R. Sassen, 2003. Two-dimensional modeling of gas hydrate decomposition in the northwestern Gulf of Mexico: Significance to global change assessment. Global and Planetary Change, 36, 31.

Milkov, A. V., 2004. Global estimates of hydrate-bound gas in marine sediments: how much is really out there? Earth Science Reviews 2004, 66, 183

Moridis, G. J., Y. Seol, and T. J. Kneafsey, 2005. Studies of reaction kinetics of methane hydrate dissociation in porous media, *Fifth International Conference on Gas Hydrates,Trondheim, Norway* 2005, *1004*, 21.

Reagan, M. T. and G. J. Moridis, 2007. Oceanic gas hydrate instability and dissociation under climate change scenarios, Geophys. Res. Letters, 34, L22709, doi:10.1029/2007GL031671

Rehder, G. S. H. Kirby, W. B. Durham, L. A. Stern, E. T. Peltzer, J. Pinkston, and P. G. Brewer, 2004. Dissolution rates of pure methane hydrate and carbon-dioxide hydrate in undersaturated seawater at 1000-m depth, Geochimica et Cosmochimica Acta, v. 68, 285-292

Ruppel, C., 2000. Thermal state of the gas hydrate reservoir in Natural gas hydrate in oceanic and permafrost environments, M.D. Max (ed.), 29-42, Kluwer Academic Publishers, Netherlands

Santamarina, J. C., F. M. Francisca, T. S. Sun, J. Y. Lee, A. I. Martin, and C. Ruppel, 2004. Mechanical, thermal, and electrical properties of hydrate bearing sediments, AAPG Hedberg Conference, Vancouver, BC, Canada, AAPG.

Severinghaus, J. P., T. Sowers, E. J. Brook, R. B. Alley, and M. L. Bender, 1998. Timing of abrupt climate change at the end of the Younger Dryas interval from thermally fractionated gases in polar ice, Nature, 391, 141.

Sloan, E. D., 1998. Clathrate Hydrates of Natural Gases, second ed. Marcel-Dekker, Inc, New York. 705 pp.

Uchida, T., S. Takeya, E. Chuvilin, R. Ohmura, J. Nagao, V. Yakushev, V. Istomin, H. Minagawa, T. Ebinuma, and H. Narita, 2004. Decomposition of methane hydrates in sand, sandstone, clays, and glass beads, Journal of Geophysical Research, v 109, B05206, doi:10.1029/2003JB002771

Uchida, T., T. Ebinuma, S. Takeya, J. Nagao, and H. Narita, 2002. Effects of pore size on dissociation temperatures and pressures of methane, carbon dioxide, and propane hydrates in porous media, Journal of Physical Chemistry B, v 106, pp. 820-826

Waite, W. F., W. J. Winters, and D. H. Mason, 2004. Methane hydrate formation in partially water-saturated Ottawa sand. Am. Mineral. 89, 1202.1207

List of Table

List of Figures

Figure 10. CT images showing effects of hydrate dissociation as the density ratio (DR) of the measured density to the water-saturated density at Slices 3, 5 13, 17, and 25. The times shown at the top of the figure are the time elapsed since the dissociation initiated. The numbers on the images (1–5) indicate the features noted in the manuscript.

Figure 11. Density ratio during hydrate dissociation monitored at Slices 5, 13, and 25. The upper plot corresponds to coarse sand and the lower plot to fine sand. “T,” “B,” and “V” stand for top, bottom, and vertical layer.

Figure 12. Average water saturation for each sand slice and type after hydrate dissociation was completed.

Figure 13. CT images showing water-saturated sand (top) and dried sand (bottom). The numbers on the images refer to the slice numbers, counted from the inlet. The darker, finger-like region and settlement in the first three slices affect previously shown saturation calculations for these slices.

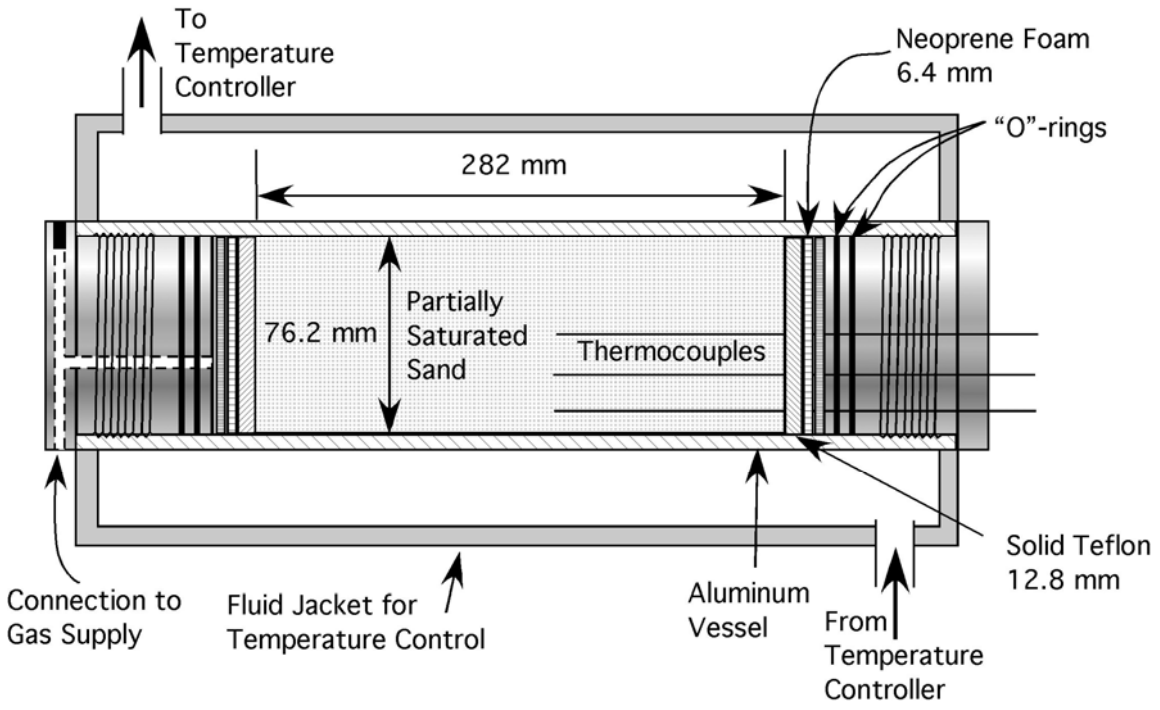

Figure 1. Experiment system schematic

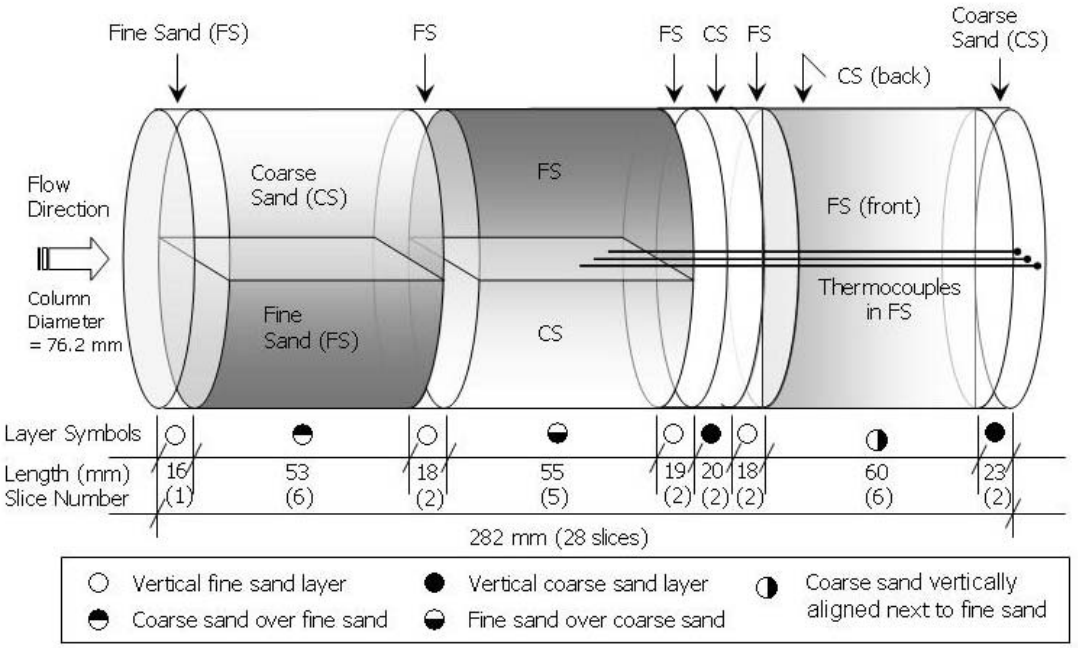

Figure 2. Layer configuration in the sand pack. Numbers at the bottom are the lengths of each column segment in millimeters with the number of CT slices in parentheses. The total number of 10 mm thick CT slices is 28. Each layer is identified by layer symbols consisting of open area (fine-grain sand) and filled area (coarse-grain sand).

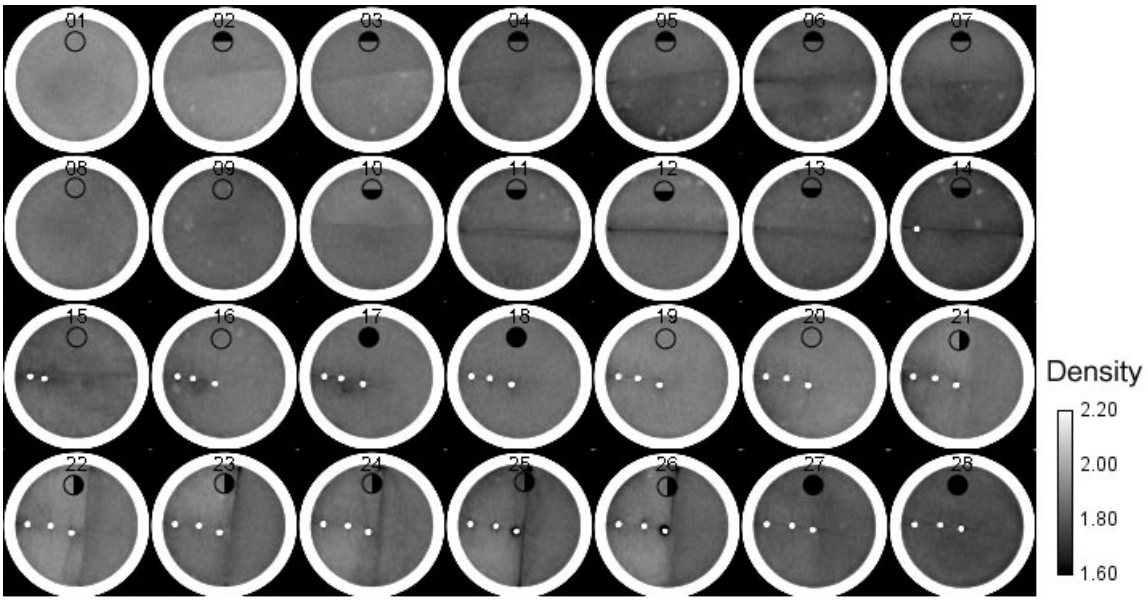

Figure 3. CT images depicting the configuration of sand layers and initial conditions prior to hydrate formation. Each of the 28 images shows density (g/cm^3) for 371 (height) × 371 (width) voxels averaged over a depth of 1 cm. The white circle is the aluminum vessel. The number on the top is the slice number starting from the inlet end. The symbol on each image represents the layer configuration, with the open area for fine sand and the filled area for coarse sand.

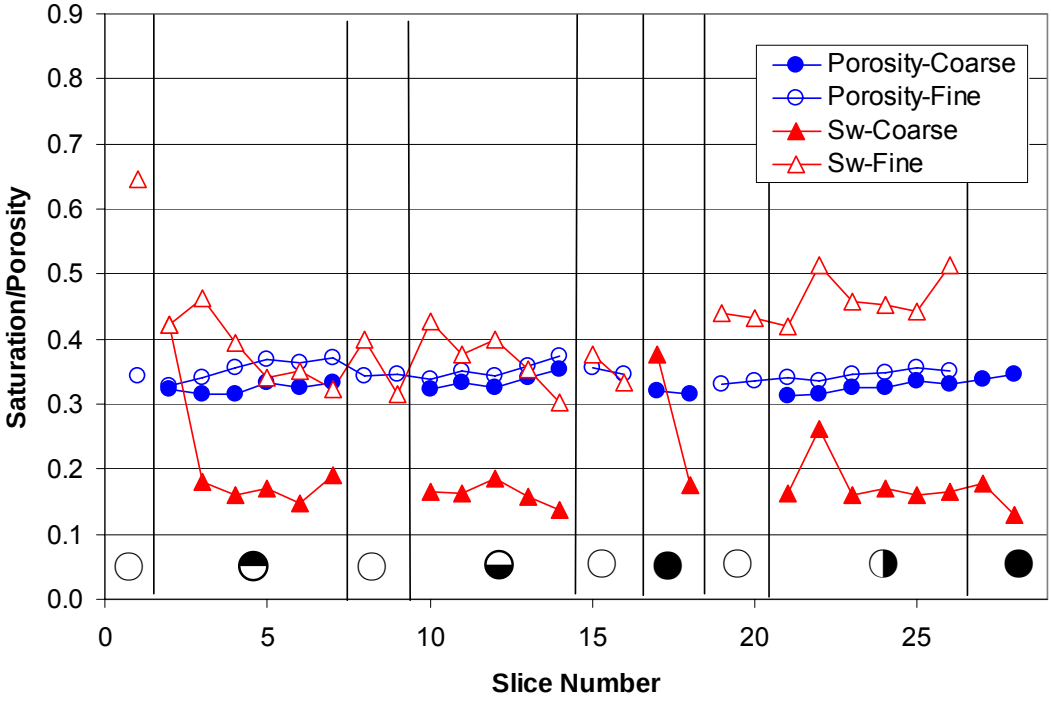

Figure 4. Average water saturation and porosity for each layer over the 28 slices. The sands with different grain sizes were separately averaged. Vertical lines show the location of column segment (or layer) boundaries.

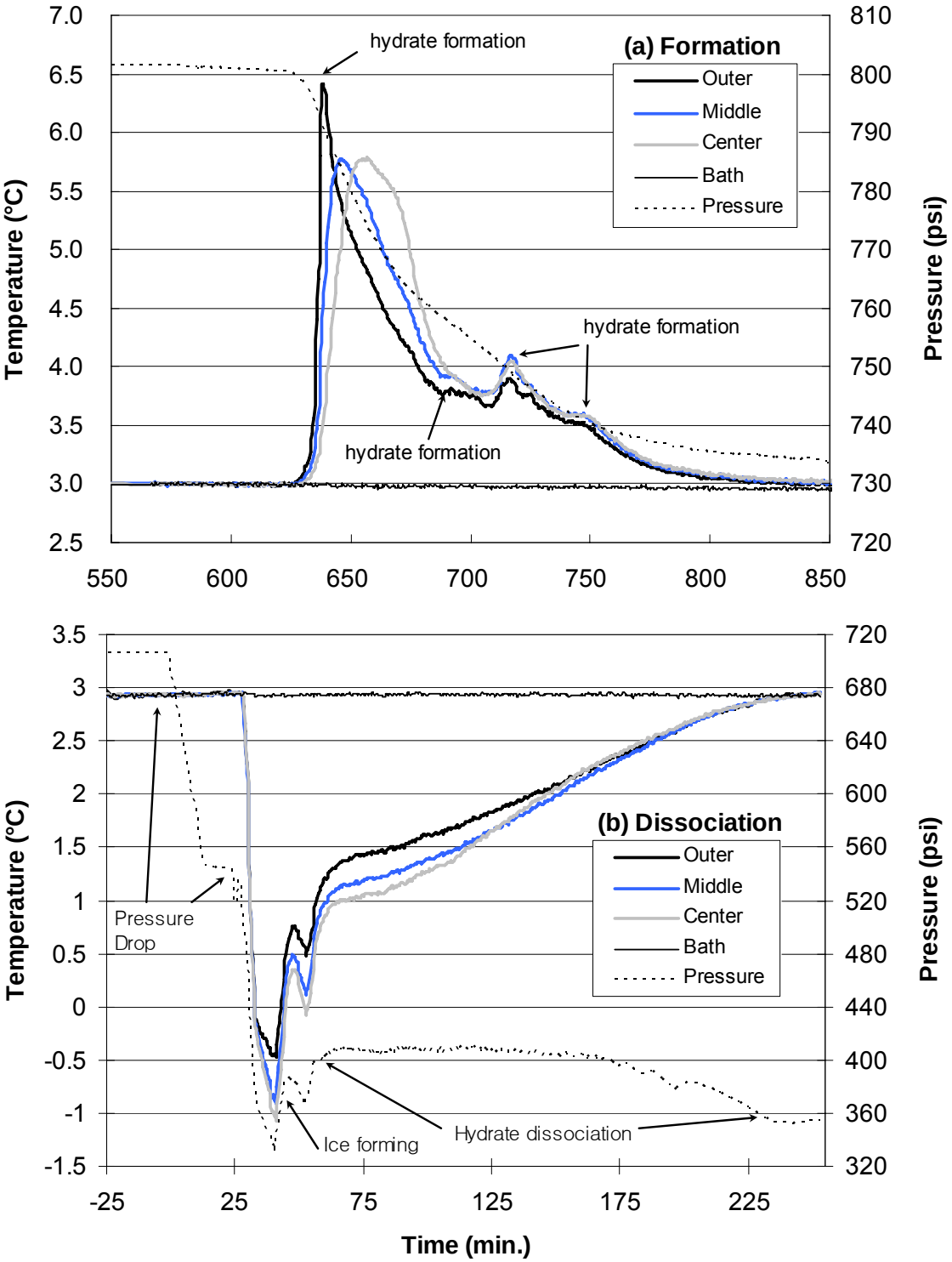

Figure 5. Temperatures and pressure during hydrate formation (a) and dissociation (b). The times on the axes were zeroed at the point when temperature was reduced for hydrate formation (top) or pressure was dropped at outlet for dissociation (bottom).

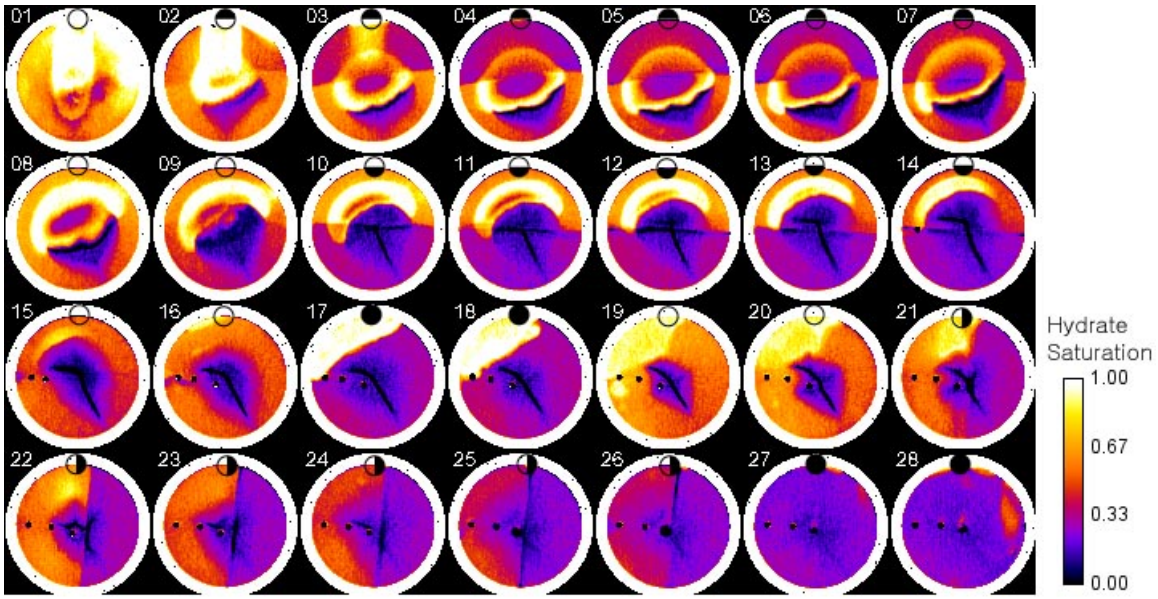

Figure 6. CT images showing hydrate saturation after the completion of hydrate formation. Circles on the top of each image represent layer configuration, with open area for fine sand and filled area for coarse sand. A brighter elliptical artifact in the first three images was caused by accidental air injection during one of the later steps of the measurement sequence (See manuscript for detailed explanation and Figure 12).

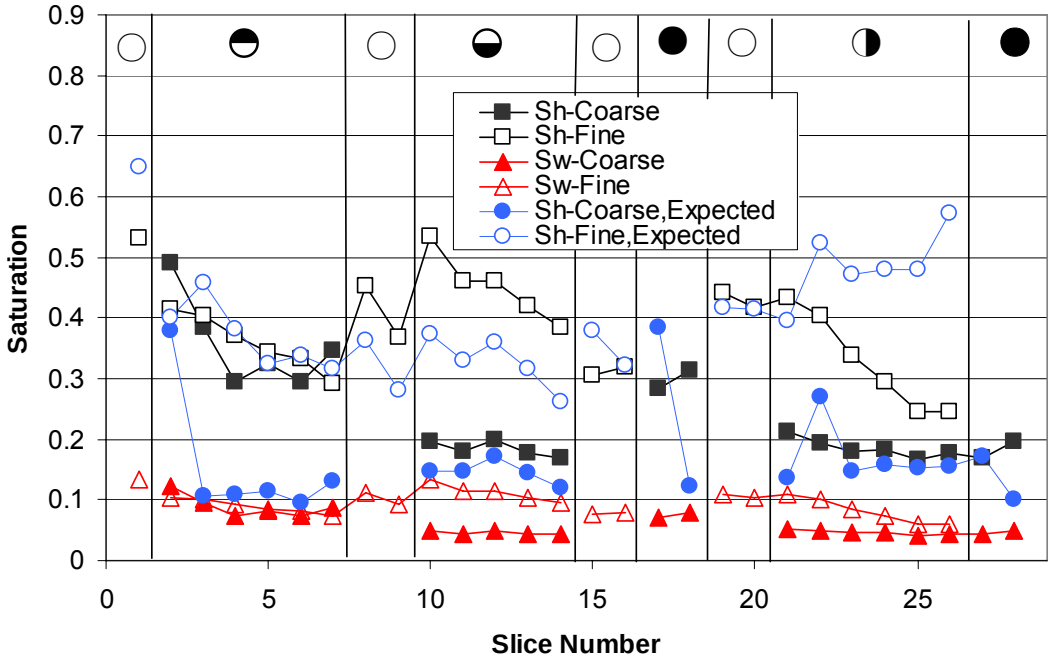

Figure 7. Average water and hydrate saturation in each slice following hydrate formation. The expected hydrate saturation for each slice is also plotted. Vertical lines show the location of column segment (or layer) boundaries.

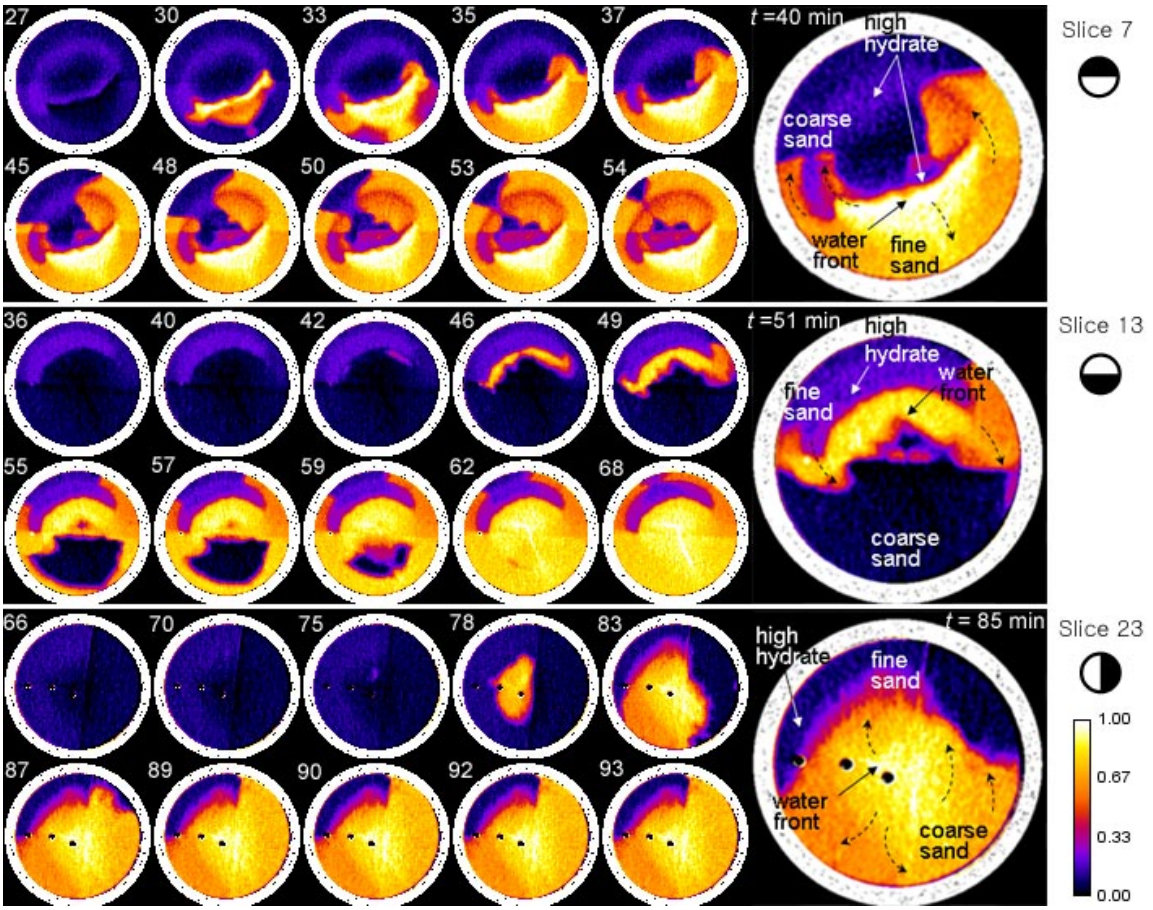

Figure 8. CT images showing temporal evolution of water saturation with water flooding at Slices 7, 13, and 23. The number at the top on each image is the time (minutes) elapsed since water injection started. The location where water breakthrough first appeared is marked as “water front”; the region with higher hydrate saturation was represented by “high hydrate.” The dotted arrow indicates where water would migrate.

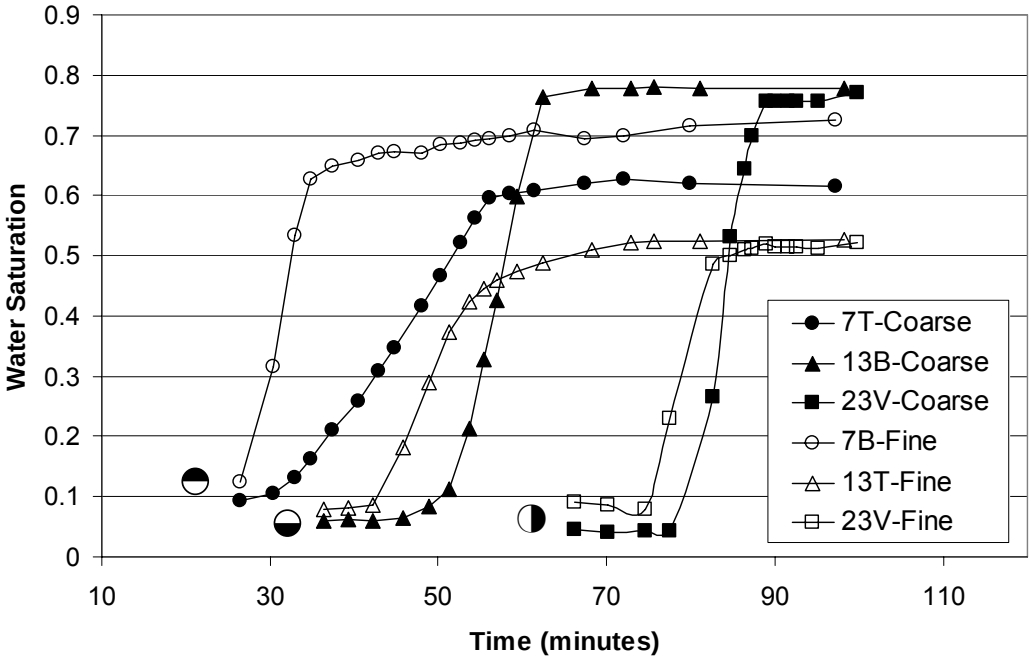

Figure 9. Water breakthrough curves at Slices 7, 13, and 23. “T,”“B,” and “V” stand for top, bottom, and vertical layer.

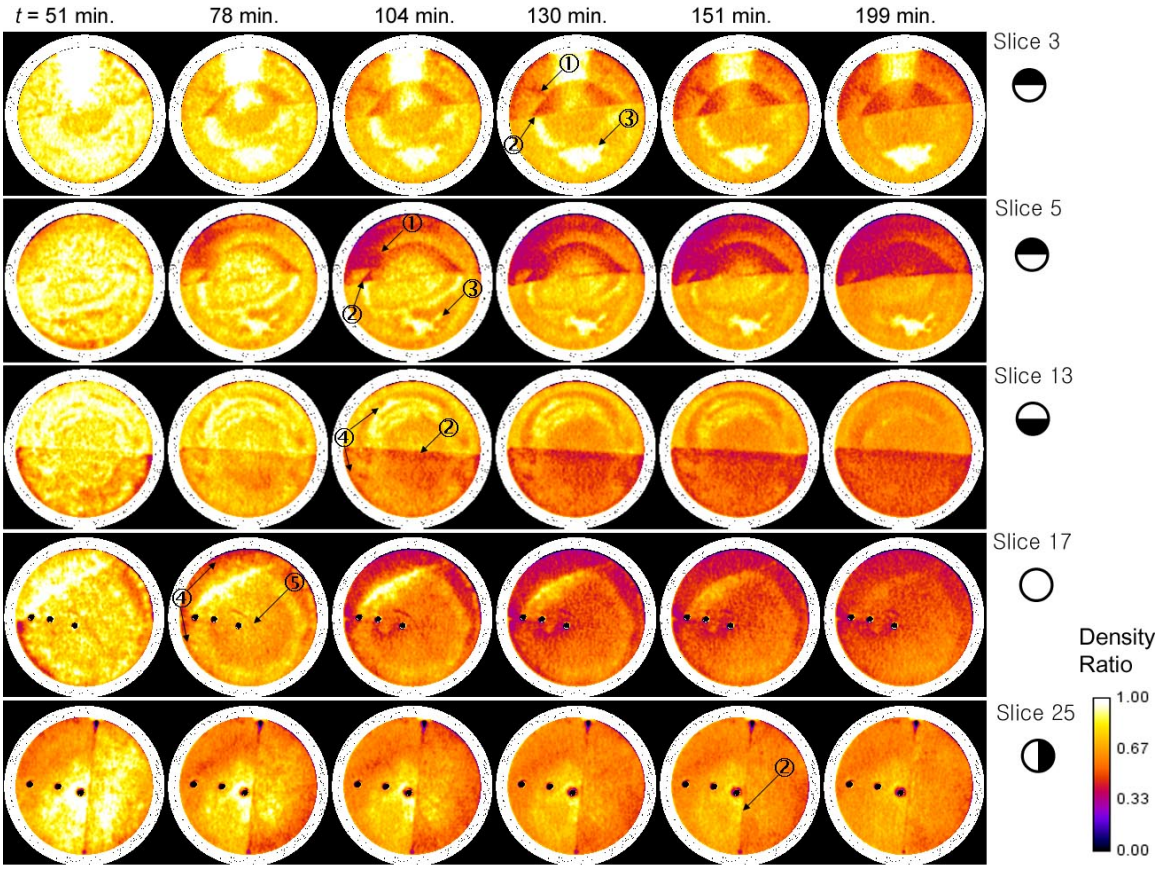

Figure 10. CT images showing effects of hydrate dissociation as the density ratio (DR) of the measured density to the water-saturated density at Slices 3, 5 13, 17, and 25. The times shown at the top of the figure are the time elapsed since the dissociation initiated. The numbers on the images (1–5) indicate the features noted in the manuscript.

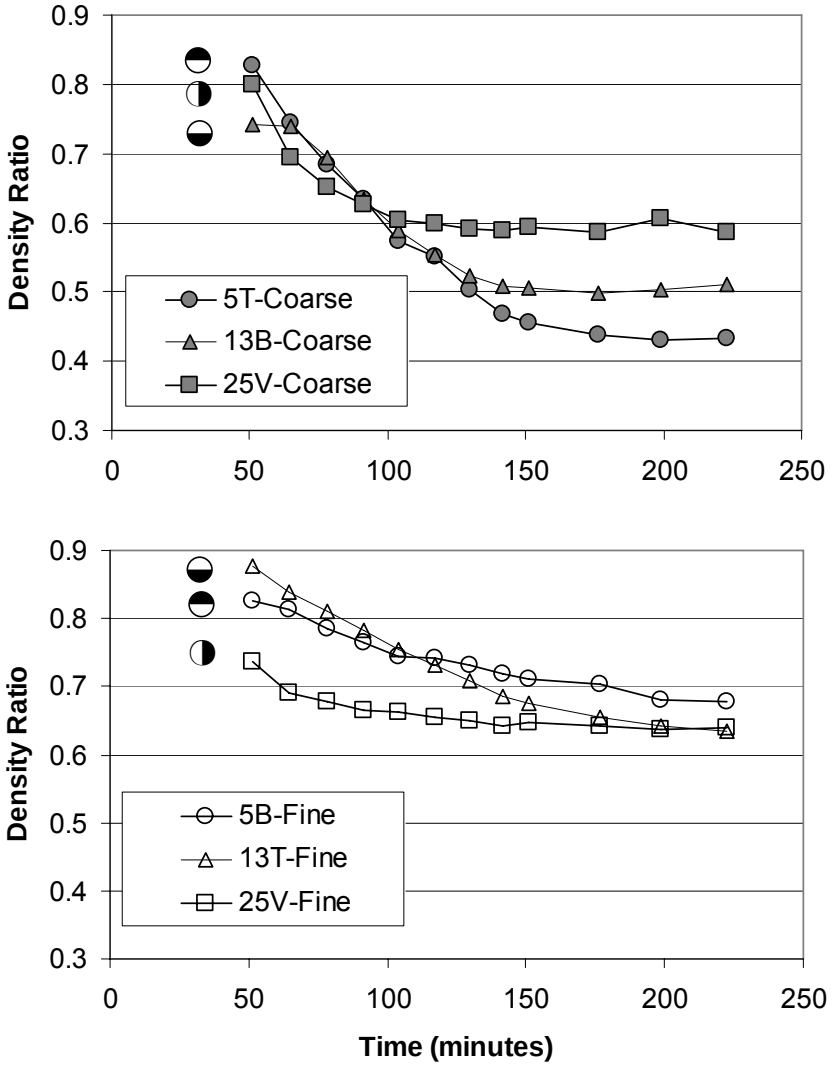

Figure 11. Density ratio during hydrate dissociation monitored at Slices 5, 13, and 25. The upper plot corresponds to coarse sand and the lower plot to fine sand. “T,” “B,” and “V” stand for top, bottom, and vertical layer.

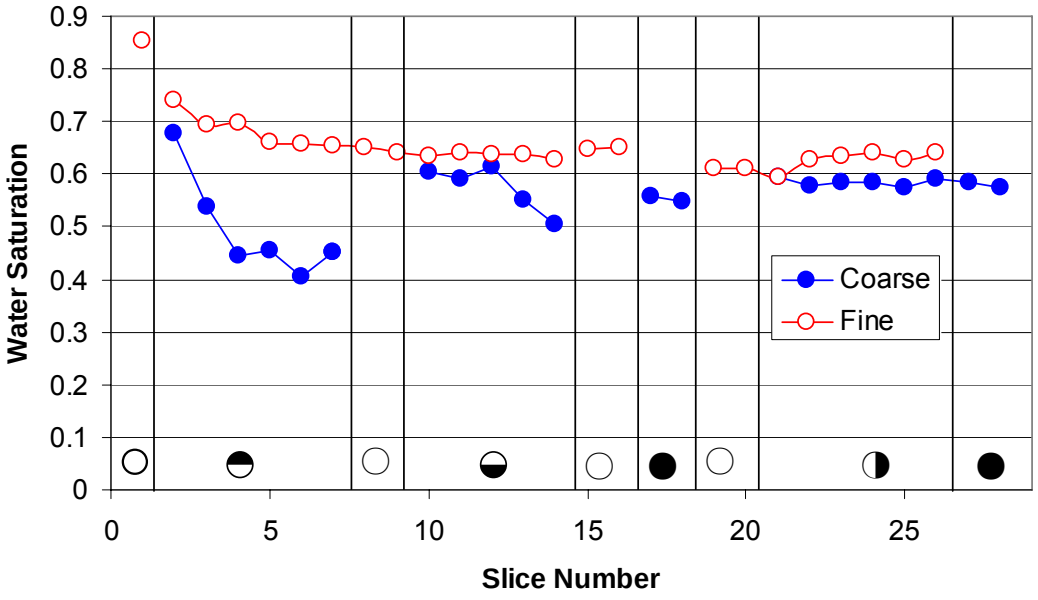

Figure 12. Average water saturation for each sand slice and type after hydrate dissociation was completed.

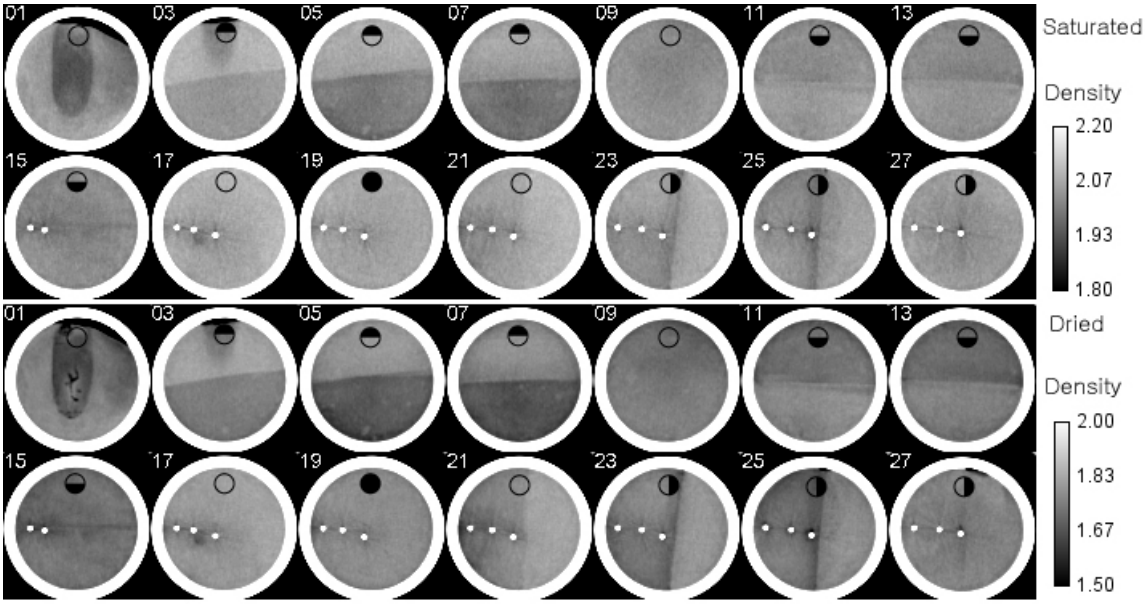

Figure 13. CT images showing water-saturated sand (top) and dried sand (bottom). The numbers on the images refer to the slice numbers, counted from the inlet. The darker finger-like region and settlement in the first three slices affect previously shown saturation calculations for these slices.